

Capturing spin-torque effects with a semilocal exchange-correlation functional

Marie-Therese Huebsch,* Fabien Tran, and Martijn Marsman
 VASP Software GmbH, Berggasse 21/14, A-1090, Vienna, Austria
 (Dated: January 9, 2025)

We cure the lack of spin torque in semilocal exchange-correlation (XC) functionals by treating XC effects in the framework of spin-current-density-functional theory (SCDFT), and present the implementation of the first kind of this novel family of XC functionals in the Vienna ab-initio simulation package (VASP): An SCDFT functional featuring a $U(1) \times SU(2)$ gauge-invariant 2×2 XC potential. While the framework can be applied to other XC functionals, the presented flavor of the SCDFT functional is based on Becke-Roussel exchange and Colle-Salvetti correlation. In addition to the 2×2 spin density and kinetic-energy density, the XC functional depends on the 2×2 spin-current density. The implementation requires the computation of the spin-current density within the projector-augmented-wave method and the variation of the XC energy with respect to it. The application to a Cr_3 molecule and bulk MnO reveals (i) spin torque of the same order as obtained by methods including exact exchange, (ii) a counterintuitive contribution to the energy even in collinear ferromagnetic systems without spin-orbit coupling due to the gradient of the magnetization, and (iii) a similar computational cost per electronic step as calculations that depend on, inter alia, the kinetic-energy density, but convergence within fewer electronic steps.

I. INTRODUCTION

Magnetic ab-initio calculations using semilocal exchange-correlation (XC) functionals suffer from a fundamental flaw: Their ignorance of spin torque. This is particularly relevant for systems featuring noncollinear magnetism, disordered magnetic moments, spin dynamics, magnetic frustration, spin waves, skyrmions, and systems with static currents such as in the presence of orbital moments, spin Hall effect, in nuclear magnetic resonance, etc. Curiously, even collinear magnetic systems may observe spin torque and, hence, already show this deficiency.

Measured by the amount of magnetic ab-initio calculations performed, the issue has been discussed relatively peripherally. To provide a balanced perspective, when Kübler *et al.* [1, 2] proposed an algorithm to treat noncollinear magnetic systems from first principles, they already pointed out that the transformation to a local spin-quantization axis only holds for the local spin-density approximation (LSDA) [3]. In other words, within LSDA the XC magnetic B-field $\vec{B}_{xc,a} = \delta E_{xc} / \delta m_a$ aligns with the magnetization \vec{m} at each point \mathbf{r} in real space and the system is therefore spin-torque-free: $\vec{m} \times \vec{B}_{xc} = 0$ for LSDA. This procedure allows determining the direction of the magnetization self-consistently within density-functional theory (DFT) [4] while evaluating the XC functional for local spin-up n_\uparrow and spin-down n_\downarrow densities, i.e., using a mere collinear, spin-polarized XC functional $E_{xc}[n_\uparrow, n_\downarrow]$ for noncollinear calculations. Figure 1(a)-(b) illustrate how the magnetization and XC B-field of an isolated Cr trimer in a traditional noncollinear calculation are absolutely parallel yielding zero spin torque.

The DFT community got used to employing XC functionals beyond the LSDA for magnetic calculations. For instance, XC functionals of the generalized gradient approximation (GGA), meta-GGA including the kinetic-energy density, or more rarely hybrid functionals, that include a fraction of Hartree-Fock exchange [5]. In fact, many implementations of noncollinear DFT allow the use of any collinear XC functional despite the missing theoretical foundation to use functionals beyond the LSDA

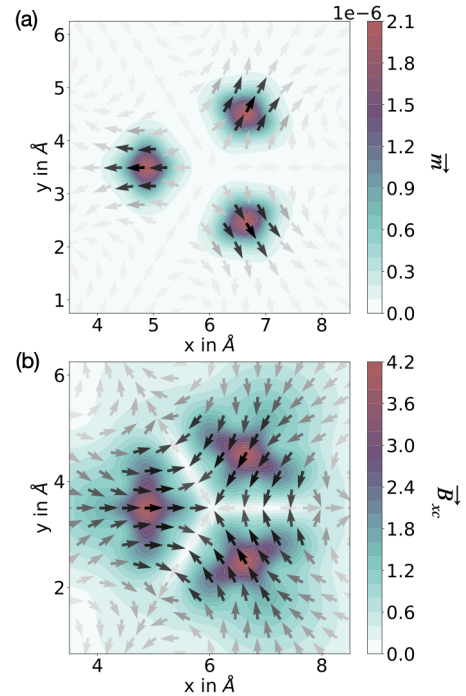


FIG. 1. (a) Magnetization \vec{m} and (b) XC magnetic B-field \vec{B}_{xc} in Cr_3 obtained from a LSDA calculation. Computational details are discussed in Section III A.

* marie-therese.huebsch@vasp.at

for noncollinear calculations. This is particularly problematic if the semilocal nature, i.e., gradient corrections, significantly influences the electronic structure and spin texture. The lack of spin torque was criticized quickly by Kleinman [6], but the first attempts at formulating a noncollinear XC functional by introducing off-diagonal elements to the XC potential led to disappointing numerical results [7].

The theoretical understanding of this failure is given in a series of works around the year 2000, where Capelle *et al.* [8–10] analyze time-dependent spin-density-functional theory (SDFT) and formulate the so-called zero-torque theorem: It states that the XC B-field cannot exert a net global spin torque on the system. Perhaps even more interesting, in the same works they established a clear *connection between the spin torque and the spin-current density*. They show that in the static limit with no external B-field and *without* spin-orbit coupling (SOC), the divergence of the tensor-valued XC spin-current density $\nabla \cdot \vec{\mathbf{J}}_{\text{xc}}$ —i.e., the difference between the many-body and Kohn-Sham (KS) currents [10]—generates a local spin torque $\vec{m} \times \vec{B}_{\text{xc}}$. This renders any spin-torque-free XC functional to be at least an approximation when studying systems governed by spin-dynamic effects, e.g., any itinerant magnet apart from the fully spin-polarized homogeneous electron gas. This shows that the spin-current density should play an integral role when extending the state-of-the-art framework of noncollinear ab-initio calculations.

It is worthwhile at this point to mention the most recent works reporting the implementation of functionals depending on the current density even if they do not necessarily focus on magnetism. Sen and Tellgren proposed a new family of functionals beyond the meta-GGA that depend also on the paramagnetic vorticity [11]. For a correct treatment of SOC, Trushin and Görling reported a fully self-consistent implementation of a general unifying theory using exact exchange (EXX) [12]. For the geometry optimization of molecules in strong magnetic fields, Irons, David, and Teale [13] implemented MGGA and hybrid functionals that depend also on the current density. Holzer, Franzke, and Pausch [14, 15], as well as Richter *et al.* [16], applied existing meta-GGA functionals with a kinetic-energy density that is augmented by a term depending on the paramagnetic current density.

Returning to our main focus, curing the lack of spin torque: A suitable guide towards proper noncollinear XC functionals are methods that map the nonlocal Hartree-Fock-exchange potential onto a local EXX potential, i.e., calculations using the optimized effective potential (OEP) method [17, 18]. However, EXX calculations come at high computational cost, rendering them unfeasible for realistic applications, yet they offer a glance at the main patterns of spin torque [19–21]. Specifically, the spin torque of the same isolated Cr trimer as shown in Fig. 1 is shown in Fig. 1(a) and (b) of Ref. [20] using (a) the Slater potential [22, 23], which is a component of the EXX potential, and (b) the more accurate Krieger-Li-

Iafrate (KLI) approximation to the EXX-OEP method [24].

In that light, thus far, approaches to formulate a noncollinear XC functional [6, 9, 20, 21, 25–34] have not proven satisfactory either because they do not obey the zero-torque theorem, neglect the spin-current density, do not reproduce the spin torque, or break the $U(1) \times SU(2)$ invariance. In an effort to overcome this limitation, we follow in this work an approach that is substantially inspired by Pittalis, Vignale, and Eich [35], and augmented by the correlation-energy functional developed by Tancogne-Dejean, Rubio, and Ullrich [20, 21]. The lack of spin torque is cured by introducing a semilocal XC functional within spin-current density functional theory (SCDFT). The complete SCDFT functional depends on the 2×2 spin density, the 2×2 kinetic-energy density, and the three vector components of the 2×2 paramagnetic spin-current density. This yields associated 2×2 partial derivatives in the expression of the 2×2 XC potential.

To the best of our knowledge, we report the first full implementation of a static noncollinear SCDFT functional, where the SDFT variational problem is extended by the variation with respect to the components of the 2×2 paramagnetic spin-current density and the XC functional explicitly provides a 2×2 potential. Intriguingly, the derivation by Pittalis, Vignale, and Eich [35] should offer a formal way of generalizing other existing functionals to noncollinear functionals yielding a non-zero local spin torque. Promising recent works on SCDFT and $U(1) \times SU(2)$ symmetry by Desmarais *et al.* [36–40] pave the way to also generalizing other XC functionals such as the strongly constrained and appropriately normed (SCAN) functionals [41–43] to be used within SCDFT in the near future. Mind that in the present work we discuss the implementation and results on noncollinear magnetism and leave the discussion of SOC effects in the context of SCDFT for prospective publications.

The article is structured as follows: In Section II the details of the implementation of the variational problem of SCDFT and the functionals expressions are given. In addition, we present a general magnetic scaling that could be applied to other XC functionals. In Section III, we most notably show the spin torque of the Cr trimer. Moreover, on the example of collinear magnetic structures of MnO, we make a comparison of (A) a simple collinear, spin-polarized calculation, (B) a traditional noncollinear calculation using a collinear XC functional, and (C) the spin-torque calculation using the novel noncollinear XC functional. Finally, we close with a summary and propose future implications in Section IV.

II. IMPLEMENTATION

The novel spin-torque algorithm is implemented into the Vienna ab-initio simulation package (VASP) [44, 45], which employs the projector augmented-wave (PAW) method [46, 47]. The 2×2 spinor-formalism required

for spin-torque calculations is presently already available to a large extent in the framework of noncollinear calculations [48]. In addition, we reuse parts of the code programmed to accommodate meta-GGAs [49].

In a nutshell, the implementation entails computing the 2×2 paramagnetic spin-current density within the PAW method and extending the variational problem to vary the total energy with respect to spin-current density. Naturally, this necessitates the introduction of the XC vector potential. Finally, the expressions for the novel SCDFE functionals are shown.

A. Variables

The starting point is the XC energy functional:

$$E_{\text{xc}} = \int d^3r e_{\text{xc}}(n_{\sigma\sigma'}, \nabla n_{\sigma\sigma'}, \nabla^2 n_{\sigma\sigma'}, \tau_{\sigma\sigma'}, \mathbf{j}_{\sigma\sigma'}), \quad (1)$$

which, in the present case, depends on the following 2×2 densities, namely the spin density

$$n_{\sigma\sigma'} = \sum_i f_i \psi_{i\sigma}^* \psi_{i\sigma'}, \quad (2)$$

where $\psi_{i\sigma}$ are the KS orbitals of the electrons and f_i the corresponding occupations, the gradient $\nabla n_{\sigma\sigma'}$ and Laplacian $\nabla^2 n_{\sigma\sigma'}$, the kinetic-energy density

$$\tau_{\sigma\sigma'} = \frac{1}{2} \sum_i f_i \nabla \psi_{i\sigma}^* \cdot \nabla \psi_{i\sigma'}, \quad (3)$$

and the paramagnetic spin-current density

$$\mathbf{j}_{\sigma\sigma'} = \frac{1}{2i} \sum_i f_i [\psi_{i\sigma}^* \nabla \psi_{i\sigma'} - (\nabla \psi_{i\sigma}^*) \psi_{i\sigma'}]. \quad (4)$$

The expressions are given in atomic units and the sums, where i is a shorthand index for the \mathbf{k} point and band, run over all states.

B. PAW expressions for the 2×2 paramagnetic spin-current density

As for any expectation value of a semilocal operator, the paramagnetic spin-current density has the following contributions:

$$\mathbf{j}_{\sigma\sigma'} = \tilde{\mathbf{j}}_{\sigma\sigma'} + \mathbf{j}_{\sigma\sigma'}^1 - \tilde{\mathbf{j}}_{\sigma\sigma'}^1. \quad (5)$$

The *valence contribution of the pseudo expectation values* on the plane-wave grid reads

$$\tilde{\mathbf{j}}_{\sigma\sigma'} = \frac{1}{2i} \sum_i f_i [\tilde{\psi}_{i\sigma}^* \nabla \tilde{\psi}_{i\sigma'} - (\nabla \tilde{\psi}_{i\sigma}^*) \tilde{\psi}_{i\sigma'}], \quad (6)$$

where $\tilde{\psi}_{i\sigma}$ are the pseudo KS orbitals. After introducing the *occupation matrix* for atomic site R and the compound indices of all local quantum numbers n and n' that go over all augmentation channels,

$$\rho_{R,nn'}^{\sigma\sigma'} = \sum_i f_i \langle \tilde{\psi}_{i\sigma'} | \tilde{p}_{Rn} \rangle \langle \tilde{p}_{Rn'} | \tilde{\psi}_{i\sigma} \rangle, \quad (7)$$

the *valence contribution of the all-electron one-center terms* on the radial grid yields

$$\mathbf{j}_{\sigma\sigma'}^1 = \frac{1}{2i} \sum_{R,nn'} \rho_{R,nn'}^{\sigma\sigma'} [\phi_{Rn}^* \nabla \phi_{Rn'} - (\nabla \phi_{Rn}^*) \phi_{Rn'}], \quad (8)$$

where ϕ_{Rn} are the all-electron partial waves that restore the nodal features of the KS orbitals within the PAW method. Likewise, the *valence contribution of the pseudo one-center terms* on the radial grid is

$$\tilde{\mathbf{j}}_{\sigma\sigma'}^1 = \frac{1}{2i} \sum_{R,nn'} \rho_{R,nn'}^{\sigma\sigma'} [\tilde{\phi}_{Rn}^* \nabla \tilde{\phi}_{Rn'} - (\nabla \tilde{\phi}_{Rn}^*) \tilde{\phi}_{Rn'}], \quad (9)$$

where the pseudo partial waves $\tilde{\phi}_{Rn}$ are identical to ϕ_{Rn} outside a certain PAW radius on site R . Thus, the all-electron and pseudo one-center terms cancel everywhere except inside a region surrounding the atoms. The core states are nonmagnetic and chosen as real, so that there is no contribution to the paramagnetic spin-current density.

C. Variational problem

With the given dependencies for the XC functional in Eq. (1), the ground-state energy can be determined by applying the variational principle to the total energy [50, 51]

$$E = \min_{n_{\sigma\sigma'}, \tau_{\sigma\sigma'}, \mathbf{j}_{\sigma\sigma'}} \left\{ F[n_{\sigma\sigma'}, \nabla n_{\sigma\sigma'}, \nabla^2 n_{\sigma\sigma'}, \tau_{\sigma\sigma'}, \mathbf{j}_{\sigma\sigma'}] + \int d^3r n v_{\text{ext}} \right\}, \quad (10)$$

where v_{ext} is the external potential, due to the nuclei and the frozen core states, and

$$F[n_{\sigma\sigma'}, \nabla n_{\sigma\sigma'}, \nabla^2 n_{\sigma\sigma'}, \tau_{\sigma\sigma'}, \mathbf{j}_{\sigma\sigma'}] = T_{\text{KS}}[n_{\sigma\sigma'}] + E_{\text{H}}[n] + E_{\text{xc}}[n_{\sigma\sigma'}, \nabla n_{\sigma\sigma'}, \nabla^2 n_{\sigma\sigma'}, \tau_{\sigma\sigma'}, \mathbf{j}_{\sigma\sigma'}] \quad (11)$$

is the universal functional, where T_{KS} is the KS kinetic energy and E_{H} is the Hartree energy. In Eqs. (10) and (11), $n = n_{\uparrow} + n_{\downarrow}$ is the total density. Essentially, the minimization of the total energy is achieved by applying the Hamilton operator to the KS orbitals which entails the application of the XC potential operator \hat{v}_{xc} onto the KS orbitals. This corresponds to a variation of the XC energy with respect to the complex-conjugate of the KS orbitals. Hence, the following terms are computed in practice:

$$\hat{v}_{\text{xc},\sigma}\psi_{i\sigma} = \frac{\delta E_{\text{xc}}}{\delta \psi_{i\sigma}^*} = \sum_{\sigma'} \left[\left(v_{\sigma\sigma'}^{\text{xc,loc}} + \nabla \cdot \frac{\mathbf{A}_{\sigma\sigma'}^{\text{xc}}}{2i} \right) \psi_{i\sigma'} - \nabla \cdot \left(\frac{\mu_{\sigma\sigma'}^{\text{xc}}}{2} \nabla \psi_{i\sigma'} \right) + \frac{\mathbf{A}_{\sigma\sigma'}^{\text{xc}}}{i} \cdot \nabla \psi_{i\sigma'} \right], \quad (12)$$

where the local component reads

$$v_{\sigma\sigma'}^{\text{xc,loc}} = \frac{\partial e_{\text{xc}}}{\partial n_{\sigma'\sigma}} - \nabla \cdot \frac{\partial e_{\text{xc}}}{\partial \nabla n_{\sigma'\sigma}} + \nabla^2 \frac{\partial e_{\text{xc}}}{\partial \nabla^2 n_{\sigma'\sigma}}, \quad (13)$$

the potential arising from the dependency on $\tau_{\sigma'\sigma}$ is given by

$$\mu_{\sigma\sigma'}^{\text{xc}} = \frac{\partial e_{\text{xc}}}{\partial \tau_{\sigma'\sigma}}, \quad (14)$$

and the nonabelian vector potential is

$$A_{\sigma\sigma',\alpha}^{\text{xc}} = \frac{\partial e_{\text{xc}}}{\partial j_{\sigma'\sigma,\alpha}}. \quad (15)$$

Here $\alpha = x, y, \text{ or } z$ is the Cartesian direction.

Note that the part of the first term and the entire last term which contain $\mathbf{A}_{\sigma\sigma'}^{\text{xc}}$ in Eq. (12) are unique to SCDFE. $v_{\sigma\sigma'}^{\text{xc,loc}}$ can be identified to the potential for pure density functionals, i.e., LSDA, GGA, and the deorbitalized MGGA functionals, e.g., SCAN-L [52]. The term in Eq. (12) involving $\mu_{\sigma\sigma'}^{\text{xc}}$ is present in usual MGGA functionals, e.g., R2SCAN [43].

D. Expressions for the exchange-correlation functional

Here, we present the detailed expressions for the non-collinear exchange and correlations functionals used in this work. They are based on the Becke-Roussel (BR89) exchange functional [53] and the Colle-Salvetti (CS) [54] correlation functional.

1. Becke-Roussel exchange functional (BR89)

Following the derivation by Pittalis *et al.* [35] yields the exchange-energy functional:

$$E_{\text{x}} = 2\pi \int d^3r n(\mathbf{r}) \int ds s h_{\text{x}}(\mathbf{r}, s), \quad (16)$$

where

$$h_{\text{x}}(\mathbf{r}, s) = - [n_{\text{top}}(\mathbf{r}) + Q_{\text{x}}(\mathbf{r})s^2 + \mathcal{O}(s^4)] \quad (17)$$

is the spherical average of the exchange-hole function

$$h_{\text{x}}(\mathbf{r}, \mathbf{r}') = - \frac{\sum_{\sigma\sigma'} \sum_i f_i \psi_{i\sigma}^*(\mathbf{r}) \psi_{i\sigma'}^*(\mathbf{r}') \sum_j f_j \psi_{j\sigma'}^*(\mathbf{r}') \psi_{j\sigma}^*(\mathbf{r})}{n(\mathbf{r})}. \quad (18)$$

This is expanded in a Taylor series at small electron-electron distance s , neglecting contributions from the fourth and higher orders in s . The on-top exchange hole at $s = 0$ reads

$$n_{\text{top}} = \sum_{\sigma\sigma'} \frac{n_{\sigma\sigma'} n_{\sigma'\sigma}}{n}, \quad (19)$$

and the exchange-hole curvature reads [55]

$$Q_{\text{x}} = \frac{1}{6} [L - 4\gamma (\bar{\tau} - \tau_{\text{W}}^{\text{nc}})]. \quad (20)$$

Here, we define the noncollinear versions of the Laplacian term

$$L = \frac{\sum_{\sigma\sigma'} n_{\sigma\sigma'} \nabla^2 n_{\sigma'\sigma}}{n}, \quad (21)$$

the noncollinear von Weizsäcker kinetic-energy density [56]

$$\tau_{\text{W}}^{\text{nc}} = \frac{\sum_{\sigma\sigma'} \nabla n_{\sigma\sigma'} \cdot \nabla n_{\sigma'\sigma}}{8n}, \quad (22)$$

and the kinetic-energy density including the paramagnetic spin-current density

$$\bar{\tau} = \frac{\sum_{\sigma\sigma'} n_{\sigma\sigma'} \tau_{\sigma'\sigma}}{n} - \frac{\sum_{\sigma\sigma'} \mathbf{j}_{\sigma\sigma'} \cdot \mathbf{j}_{\sigma'\sigma}}{2n}. \quad (23)$$

To fulfill the homogeneous electron gas limit the parameter γ in Eq. (20) has to be set to $\gamma = 0.8$ [53].

Alternatively to Eq. (20), the exchange-hole curvature can be given by [35]

$$\tilde{Q}_{\text{x}} = \frac{1}{6} [-8\tau_{\text{W}}^{\text{nc}} - 4\gamma (\bar{\tau} - \tau_{\text{W}}^{\text{nc}})] \quad (24)$$

after integrating Eq. (16) by part to get rid of the Laplacian term. This is numerically favorable and indeed used

in the implementation. One could even define a version fully independent of $\tau_{\text{W}}^{\text{ncl}}$, which yields

$$\bar{Q}_x = \frac{1}{6} \left[L - 4\gamma \left(\bar{\tau} + \frac{1}{8}L \right) \right]. \quad (25)$$

We will refer to this equation in the discussion of the correlation energy.

Then, based on Eq. (19) and either Eq. (20), Eq. (24) or Eq. (25) the usual Becke-Roussel expressions [53] can be employed, leading to

$$E_x = \frac{1}{2} \int d^3r n(\mathbf{r})U(\mathbf{r}), \quad (26)$$

where

$$U = -2(\pi n_{\text{top}})^{1/3} e^{x/3} \frac{1 - e^{-x} \left(1 + \frac{1}{2}x\right)}{x}, \quad (27)$$

where x is obtained by solving the following nonlinear one-dimensional equation that has no simple algebraic solution:

$$\frac{x e^{-2x/3}}{x-2} = \frac{2}{3} \pi^{2/3} \frac{n_{\text{top}}^{5/3}}{\bar{Q}_x}. \quad (28)$$

To inspect the nonmagnetic limit it is useful to rewrite the above quantities in spinor space in the basis spanned by the 2×2 unit matrix and the Pauli matrices σ_a with $a = 1, 2, 3$. This way, the relevant quantities, defined in Eqs. (19), (22) and (23), are given in terms of their charge and magnetization contributions:

$$n_{\text{top}} = \frac{n}{2} \left(1 + \frac{\sum_a m^a m^a}{n^2} \right), \quad (29)$$

$$\tau_{\text{W}}^{\text{ncl}} = \frac{\tau_{\text{W}}}{2} \left(1 + \frac{\sum_a |\nabla m^a|^2}{|\nabla n|^2} \right), \quad (30)$$

where

$$\tau_{\text{W}} = \frac{|\nabla n|^2}{8n} \quad (31)$$

and

$$\bar{\tau} = \frac{\tau}{2} \left(1 + \frac{\sum_a m^a \tau_m^a}{n\tau} \right) - \frac{|\mathbf{j}|^2}{4n} \left(1 + \frac{\sum_a |\mathbf{J}^a|^2}{|\mathbf{j}|^2} \right). \quad (32)$$

Mind that the magnetization \vec{m} is a spinor quantity and not a vector-like quantity such as the charge current \mathbf{j} . Thus, the magnetic current $\vec{\mathbf{J}}$ is a tensor connecting spinor and vectorial quantities, which in ordinary SDFT only happens via SOC. Based on Eqs. (29), (30) and (32), the nonmagnetic limits are deduced:

$$\lim_{m^a \rightarrow 0} n_{\text{top}} = \frac{n}{2}, \quad (33)$$

$$\lim_{m^a \rightarrow 0} \tau_{\text{W}}^{\text{ncl}} = \frac{\tau_{\text{W}}}{2}, \quad (34)$$

$$\lim_{m^a \rightarrow 0} \bar{\tau} = \frac{1}{2} \left(\tau - \frac{|\mathbf{j}|^2}{2n} \right), \quad (35)$$

which leads to the following nonmagnetic limit for \bar{Q}_x :

$$\lim_{m^a \rightarrow 0} \bar{Q}_x = \frac{1}{12} \left[-8\tau_{\text{W}} - 4\gamma \left(\tau - \frac{|\mathbf{j}|^2}{2n} - \tau_{\text{W}} \right) \right]. \quad (36)$$

In our implementation, we use \bar{Q}_x as defined in Eq. (24), because the second derivatives of the density, required to compute the Laplacian introduce significant noise in the XC potential. Nevertheless for the sake of completeness, the Laplacian in charge and magnetization representation and the corresponding nonmagnetic limit are

$$L = \frac{\nabla^2 n}{2} \left(1 + \frac{\sum_a m^a \nabla^2 m^a}{n \nabla^2 n} \right), \quad (37)$$

$$\lim_{m^a \rightarrow 0} L = \frac{\nabla^2 n}{2}, \quad (38)$$

and

$$\lim_{m^a \rightarrow 0} Q_x = \frac{1}{12} \left[\nabla^2 n - 4\gamma \left(\tau - \frac{|\mathbf{j}|^2}{2n} - \tau_{\text{W}} \right) \right]. \quad (39)$$

2. Colle-Salvetti correlation functional (CS)

Based on the following ansatz for the many-body wavefunction by Colle and Salvetti [54]

$$\begin{aligned} \Psi(\mathbf{r}_1\sigma_1, \dots, \mathbf{r}_N\sigma_N) \\ = \Psi_{\text{HF}}(\mathbf{r}_1\sigma_1, \dots, \mathbf{r}_N\sigma_N) \prod_{i>j} [1 - \varphi(\mathbf{r}_i, \mathbf{r}_j)], \end{aligned} \quad (40)$$

and the definitions of the Hartree-Fock one and two-electron reduced density matrices [57]

$$\rho_{1\text{HF}}^{\sigma_1\sigma'_1}(\mathbf{r}_1, \mathbf{r}'_1) = N \sum_{\sigma_2, \dots, \sigma_N} \int \Psi_{\text{HF}}(\mathbf{r}_1\sigma_1, \mathbf{r}_2\sigma_2, \dots, \mathbf{r}_N\sigma_N) \Psi_{\text{HF}}^*(\mathbf{r}'_1\sigma'_1, \mathbf{r}_2\sigma_2, \dots, \mathbf{r}_N\sigma_N) d^3r_2 \dots d^3r_N, \quad (41)$$

$$\rho_{2\text{HF}}^{\sigma_1\sigma_2\sigma'_1\sigma'_2}(\mathbf{r}_1, \mathbf{r}_2; \mathbf{r}'_1, \mathbf{r}'_2) = N(N-1) \sum_{\sigma_3, \dots, \sigma_N} \int \Psi_{\text{HF}}(\mathbf{r}_1\sigma_1, \mathbf{r}_2\sigma_2, \mathbf{r}_3\sigma_3, \dots, \mathbf{r}_N\sigma_N) \Psi_{\text{HF}}^*(\mathbf{r}'_1\sigma'_1, \mathbf{r}'_2\sigma'_2, \mathbf{r}_3\sigma_3, \dots, \mathbf{r}_N\sigma_N) d^3r_3 \dots d^3r_N, \quad (42)$$

where $\rho_{1\text{HF}}(\mathbf{r}, \mathbf{r}) = n(\mathbf{r})$, Colle and Salvetti [54] formulate an approximate form for the correlation energy:

$$E_c = -2a \int \frac{\rho_{2\text{HF}}(\mathbf{r}, \mathbf{r}, \mathbf{r}, \mathbf{r})}{n(\mathbf{r})} \frac{1 + bn(\mathbf{r})^{-8/3} \nabla_{\mathbf{s}}^2 \rho_{2\text{HF}}(\mathbf{r} - \frac{\mathbf{s}}{2}, \mathbf{r} + \frac{\mathbf{s}}{2}, \mathbf{r} - \frac{\mathbf{s}}{2}, \mathbf{r} + \frac{\mathbf{s}}{2})|_{\mathbf{s}=0}}{1 + dn(\mathbf{r})^{-1/3}} e^{-cn(\mathbf{r})^{-1/3}} d^3r. \quad (43)$$

Here, the parameters $a = 0.04918$, $b = 0.06598$, $c = 0.25328$, and $d = 0.34935$ were fitted to the exact solution for the He atom at various distances by Colle and Salvetti [54].

A nonmagnetic density functional can be derived using the approximation proposed by Lee, Yang, and Parr [58]

$$\rho_{2\text{HF}}(\mathbf{r}_1, \mathbf{r}_2; \mathbf{r}_1, \mathbf{r}_2) = n(\mathbf{r}_1)n(\mathbf{r}_2) - \frac{1}{2}\rho_{1\text{HF}}(\mathbf{r}_1, \mathbf{r}_2)\rho_{1\text{HF}}(\mathbf{r}_2, \mathbf{r}_1). \quad (44)$$

For a noncollinear version, we use the same approximation as proposed by Tancogne-Dejean, Rubio, and Ullrich [20, 21]

$$\rho_{2\text{HF}}(\mathbf{r}_1, \mathbf{r}_2; \mathbf{r}_1, \mathbf{r}_2) = n(\mathbf{r}_1)n(\mathbf{r}_2) - \sum_{\sigma_1\sigma_2} \rho_{1\text{HF}}^{\sigma_1\sigma_2}(\mathbf{r}_1, \mathbf{r}_2)\rho_{1\text{HF}}^{\sigma_2\sigma_1}(\mathbf{r}_2, \mathbf{r}_1), \quad (45)$$

which consists of the Hartree contribution minus an exchange contribution.

In agreement with Tancogne-Dejean, Rubio, and Ullrich [20, 21], we find that [59]

$$\rho_{2\text{HF}}(\mathbf{r}, \mathbf{r}, \mathbf{r}, \mathbf{r}) = n^2 - nn_{\text{top}}, \quad (46)$$

where n_{top} is defined in Eqs. (19) and (29), and

$$\nabla_{\mathbf{s}}^2 \rho_{2\text{HF}}\left(\mathbf{r} - \frac{\mathbf{s}}{2}, \mathbf{r} + \frac{\mathbf{s}}{2}, \mathbf{r} - \frac{\mathbf{s}}{2}, \mathbf{r} + \frac{\mathbf{s}}{2}\right)\Big|_{\mathbf{s}=0} = \frac{n\nabla^2 n}{2} - 4n\tau_{\text{W}} - \left(\frac{nL}{2} - 4n\bar{\tau}\right), \quad (47)$$

where L is defined in Eqs. (21) and (37), $\bar{\tau}$ in Eqs. (23) and (32) and τ_{W} in Eq. (31). Here, we can identify the exchange-hole curvature

$$\frac{nL}{2} - 4n\bar{\tau} = 6n\bar{Q}_x^{\gamma=1} \quad (48)$$

by comparison of Eqs. (25) and (47) with $\gamma = 1$. Finally, this yields the expression for the correlation energy (same as Eq. (14) in Ref. [20]):

$$E_c = -2a \int (n - n_{\text{top}}) \frac{1 + bn^{-5/3} \left(\frac{\nabla^2 n}{2} - 4\tau_{\text{W}} - 6\bar{Q}_x^{\gamma=1}\right) e^{-cn^{-1/3}}}{1 + dn^{-1/3}} d^3r. \quad (49)$$

In fact, integration by parts can be exploited to replace $\bar{Q}_x^{\gamma=1}$ with $Q_x^{\gamma=1}$ or $\tilde{Q}_x^{\gamma=1}$ that are defined in Section IID 1. This is not obvious from the final form of E_c in Eq. (49) but follows from the derivation of Colle and Salvetti [54].

In the nonmagnetic limit, we obtain

$$\lim_{m^a \rightarrow 0} (n - n_{\text{top}}) = \frac{n}{2} \quad (50)$$

$$\begin{aligned} \lim_{m^a \rightarrow 0} \left(\frac{\nabla^2 n}{2} - 4\tau_{\text{W}} - 6\bar{Q}_x^{\gamma=1} \right) \\ = \frac{\nabla^2 n}{4} - 4\tau_{\text{W}} + 2 \left(\tau - \frac{|\mathbf{j}|^2}{2n} \right). \end{aligned} \quad (51)$$

Inserting Eqs. (50) and (51) in Eq. (49) recovers the nonmagnetic case discussed by Lee, Yang, and Parr, see Eq. (10) of Ref. [58].

E. Application to other exchange-correlation functionals

In the course of analyzing the nonmagnetic limit in the previous sections, we could see in Eqs. (29), (30), (32) and (37) that each quantity has a general magnetic scaling behavior with respect to the nonmagnetic limit. This is distinct from the spin-scaling relation that is usually used to construct spin-polarized semi-local XC functionals [60]. In order to generalize other XC functionals to the noncollinear case, one has to identify parts that originate from the on-top exchange hole and the exchange curvature. Although the substitution of n and τ suggested by Pittalis *et al.* [35], would be very elegant, generally in practice one ought to consider if the contribution is due to an exchange process and only apply magnetic scaling to those terms. For instance, in the Colle-Salvetti correlation functional discussed in Eq. (45) the second contribution on the right side corresponds to an exchange process. In addition, one should consider the terms in the curvature individually to avoid accidentally breaking $U(1)\times SU(2)$ symmetry [61].

III. APPLICATIONS

We selected two systems to illustrate the particular characteristics of the first SCDFE functional including spin-torque effects implemented in the VASP code: An isolated Cr_3 molecule and bulk antiferromagnetic MnO, that are noncollinear and collinear magnetic systems, respectively.

A. Cr_3 molecule

The Cr trimer is a common example to illustrate noncollinear magnetization [2, 48] and the presence of spin torque [19–21]. Here, we focus on the spin torque and on-site magnetic moment computed by means of the novel SCDFE-BR89-CS functional in comparison to other widely used XC functionals.

The computational details of the calculations on Cr_3 —presented in Figs. 1 and 2 and Table I—are as follows: The molecule is placed in a hexagonal cell as a monolayer, where the interlayer distance, as well as the distance between the centers of neighboring trimers is 8 Å. The inter-atomic distance is 2 Å. The structural parameters are chosen such that the results can be compared to those in Ref. [20, 21]. The calculations are performed at the Γ point and with a cutoff energy of 35.28 Ry for the plane-wave basis. The magnetic moments on the Cr atoms are initialized to point outwards and remain in

that orientation after electronic relaxation. The magnetization and the XC B-field in Figs. 1 and 2 are shown at every 6th grid point in real space and we zoom into the relevant region with high electron density, i.e., we omit showing the vacuum region. We report that the magnetization and XC B-field for LSDA and SCDFE-BR89-CS are well behaved in the vacuum region and show no noise or unphysical values.

Remarkably, in Fig. 2 we can recognize similar patterns in the spin torque of SCDFE-BR89-CS as in the more involved calculations shown in Fig. 1(a), for Slater, and (b), for EXX-KLI, of Ref. [20, 21]. In contrast to the noncollinear XC functional (also based on BR89 and CS) implemented in Ref. [20, 21] that is shown in Fig. 1 (c) therein, we see a smooth behavior of the spin torque on the Cr sites. Our approach to constructing the SCDFE-BR89-CS functional is different from the approach reported in Ref. [20, 21] in the following key aspects: Namely, (i) our expression for the SCDFE-BR89 exchange energy substitutes the exchange-hole curvature Q rather than the kinetic energy τ to avoid breaking $U(1)\times SU(2)$ invariance, (ii) we performed an integration by part to avoid the presence of the Laplacian of the density in the SCDFE-BR89 exchange energy, and (iii) the SCDFE variational problem also optimizes with respect to the three components of the 2×2 paramagnetic spin-current density. Thus, both the XC functional and the variational problem are distinct from Ref. [20, 21].

Strikingly, in Fig. 2, four distinct regions of a larger magnitude can be observed at each site, which shows a resemblance to the EXX-KLI result of Ref. [20]. Although no symmetry is imposed during the spin-torque calculation, the total spin torque vanishes. Therefore, the zero-torque theorem by Capelle *et al.* [10] is fulfilled. The sign changes in the same pattern, with adjacent regions on the same site observing the opposite sign. The sign of the spin torque of our calculations agrees with the sign of Slater and EXX-KLI results in the center of the three Cr atoms, but curiously, on-site, the sign is the opposite. In between the center of the molecule and the on-site regions, there is a very thin stripe where the sign

TABLE I. On-site magnetic moment μ in μ_B of an isolated Cr_3 molecule for different XC functionals representative of the various families of functionals.

XC functional	μ (μ_B)
SCDFE-BR89-CS	3.15(5)
MGGA-BR89-CS ($\mathbf{m} \times \mathbf{B}_{xc} \equiv 0$, $\mathbf{j}_{\sigma\sigma'} \equiv 0$)	3.16(3)
LSDA-PZ	1.68
GGA-PBE	2.15
MGGA-R2SCAN	2.95
Hybrid-HSE06	3.32
EXX-KLI	3.81 ^a
Hartree-Fock	4.07

^a Reference [20]

changes. Thus, it does not appear to be the on-site region that extends toward the center of the molecule but a more involved pattern similar to what is observed with the Slater potential [20]. We speculate that different XC functionals within SCDFD may yield different patterns, yet the common features among the SCDFD-BR89-CS, EXX and EXX-KLI calculations are already compelling.

Table I lists the on-site spin magnetic moment μ extracted by projection onto the one-center PAW functions. In addition to the values obtained with SCDFD-BR89-CS, the results obtained from various other XC functionals representative for each family of functionals are also shown. These are (i) the LSDA Slater exchange [62] combined with Perdew-Zunger parametrization [63] of Ceperley-Alder Monte Carlo correlation data for the homogeneous electron gas [64] (LSDA-PZ), (ii) the Perdew-Burke-Ernzerhof GGA (GGA-PBE) [65] functional, (iii) the second regularized version of the strongly constrained and appropriately normed functional [43] (MGGA-R2SCAN), (iv) the Heyd-Scuseria-Ernzerhof screened hybrid functional [66, 67] (HSE06), and finally (v) the Hartree-Fock approximation.

The results show that SCDFD-BR89-CS leads to a moment, $\mu = 3.16 \mu_B$, that is relatively close to the values obtained with MGGA-R2SCAN ($\mu = 2.95 \mu_B$) and HSE06 ($\mu = 3.32 \mu_B$). They are much larger than the values obtained with LSDA-PZ ($\mu = 1.68 \mu_B$) and GGA-PBE ($\mu = 2.15 \mu_B$). It is rather common that functionals of the meta-GGA and hybrid families increase the magnetic moment with respect to the standard LSDA-PZ and GGA-PBE, see e.g., Refs. [68–70] for calculations on simple ferromagnetic metals and antiferromagnetic transition-metal monoxides. At the other extreme, the Hartree-Fock approximation leads to a much larger moment of $4.07 \mu_B$. This is rather similar to $3.81 \mu_B$

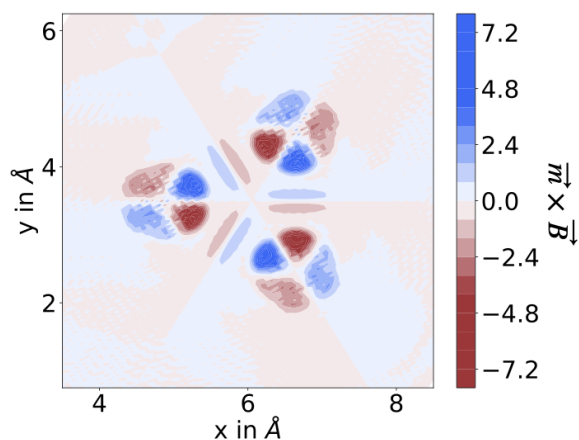


FIG. 2. Magnitude of the spin torque $\vec{m} \times \vec{B}_{xc}$ in 10^3 a.u. along the out-of-plane direction for an isolated Cr trimer using the semilocal spin-current-density-functional-theory (SCDFD) version of Becke-Roussel 89 exchange combined with the Colle-Salvetti correlation, SCDFD-BR89-CS, implemented in VASP.

obtained by the related EXX-KLI method [20]. Mind that generally, the value of the on-site magnetic moment is sensitive to the exact definition and implementation of the on-site magnetic moment in each code. However, as both LSDA-PZ and Hartree-Fock in Ref. [20] closely agree with our values, we may point out that Tancogne-Dejean, Rubio, and Ullrich obtained a magnetic moment of $2.45 \mu_B$, see Erratum [21], with their BR89-CS-based noncollinear functional. A value that is significantly smaller than our SCDFD-BR89-CS value.

As a side remark, we may mention here that hybrid functionals implicitly include spin-torque effects via the nonlocal Fock potential. However, noncollinear calculations using hybrid functionals are still problematic because the semilocal part is based on a collinear spin-polarized GGA. Recall that any not entirely local contribution to the XC energy, such as the gradient, leads to a finite spin torque, which has already been recognized by Kübler *et al.* [1].

By setting the off-diagonal elements $(\sigma, \sigma') = (\uparrow, \downarrow)$ and (\downarrow, \uparrow) of the 2×2 densities ($n_{\sigma, \sigma'}$, $\tau_{\sigma, \sigma'}$, etc.) to zero, we obtain a collinear version of the BR89-CS functional. In other words, we define a collinear spin-polarized XC functional via the magnetic scaling described in section II E. This is fundamentally distinct from using the spin-scaling relation [60] to obtain a collinear XC functional. Yet, it allows performing a noncollinear calculation the traditional way, i.e., by rotating the XC B-field to align it with the noncollinear magnetization self-consistently. This enforces the spin-torque to vanish everywhere in space, $\vec{m} \times \vec{B}_{xc} \equiv 0$. Moreover, setting also the current density to zero, $\mathbf{j}_{\sigma\sigma'} \equiv 0$, leads to a MGGA which we refer to as MGGA-BR89-CS in Table I.

In Table I, we see that the MGGA-BR89-CS magnetic moment is the same as for SCDFD-BR89-CS. More dramatic is the change in the total energy: The total energy of MGGA-BR89-CS is lower than SCDFD-BR89-CS by about 0.05 eV. This large difference is unlikely due to the small change in the on-site magnetic moment. Setting only $\mathbf{j}_{\sigma\sigma'} \equiv 0$ affects neither the total energy nor the size of the magnetic moment in case of Cr₃, so we omit listing enforcing only $\vec{m} \times \vec{B}_{xc} \equiv 0$ or only $\mathbf{j}_{\sigma\sigma'} \equiv 0$ separately in Table I. Hence, the energy difference of 0.05 eV is due to the spin-density being constrained to a subspace, where the underlying physics obeys SCDFD.

The expected magnitude of the spin torque may be scaled by $a = \mu_{\text{SCDFD}}/\mu_{\text{EXX-KLI}} \approx 0.83$, considering that the magnetic moment of SCDFD-BR89-CS is smaller than the magnetic moment in EXX-KLI, see Table I. In practice, we find $b = \max(\vec{m} \times \vec{B}_{xc})_{\text{SCDFD}}/\max(\vec{m} \times \vec{B}_{xc})_{\text{EXX}} \approx 0.75$. Hence, SCDFD-BR89-CS captures roughly $b/a \approx 90\%$ of the spin torque present in EXX-KLI for Cr₃.

In summary, the pattern of the spin torque of SCDFD-BR89-CS shows four on-site regions similar to EXX-KLI from Ref. [20]. However, the detailed shape and sign of the regions depend on the XC functional. The magnitude of the on-site magnetic moment is close to the values of

MGGA-R2SCAN and hybrid-HSE06. Relative to that, SCDF-T-BR89-CS yields about 90% of the spin torque as expected based on EXX-KLI. The total energy changes significantly for the same XC functional if $\vec{m}(\mathbf{r}) \parallel \vec{B}_{\text{xc}}(\mathbf{r})$ is imposed ad hoc. In other words, taking the zero-local-spin-torque limit of an MGGA functional is a radical approximation.

B. Rocksalt antiferromagnetic MnO

The discussion of the new SCDF-T-BR89-CS functional based on MnO is motivated by two aspects: (i) Archer, *et al.* [75] show analogous results for a range of XC functionals including hybrid-HSE06 and GGA-PBE, and (ii) the possibility to apply all three available modes for a magnetic calculation:

- (A) A collinear spin-polarized calculation using both a collinear spin-polarized XC functional and algorithm.
- (B) A traditional noncollinear calculation using a collinear spin-polarized XC functional with a noncollinear algorithm.
- (C) A spin-torque calculation using a noncollinear XC functional with a noncollinear algorithm.

The considered ferromagnetic (FM) and two different antiferromagnetic (AFM) magnetic configurations are shown in Fig. 3(a)-(c). Naively, one would expect that such collinear systems with negligible SOC are well-described with a simple collinear calculation corresponding to (A) which would make any differences compared to (B) and/or (C) rather intriguing.

The computational details for the calculations presented in Fig. 3 and Table II are as follows: The FM and AFM1 structures consist of 8 atomic sites in the conventional unit cell, while the cell of AFM2 is chosen by considering the Mn sites on the diagonal in Fig. 3(c), i.e., the lower left and upper right Mn sites as well as the central O site and the O site in extension of the diagonal that is not shown in the figure. The lattice constant a is varied from 3.8 to 4.7 Å. In combination with these structures, the k-point mesh for the integration into the Brillouin zone is $8 \times 8 \times 8$ for FM and AFM1, and $4 \times 4 \times 4$ for AFM2. The calculations are performed at a cutoff energy of 38.22 Ry for the plane-wave basis. The magnetic moments are initialized as shown in Fig. 3(a)-(c), and no symmetrization is applied.

Figure 3(d)-(f) displays the characteristic patterns of the spin torque corresponding to the magnetic configurations shown in Fig. 3(a)-(c), respectively. The spin torque is exceedingly small as it is five orders of magnitude smaller than in Cr₃. This indicates that the zero-spin-torque limit is indeed a good approximation, which is discussed in more detail below. Despite the small magnitude, the patterns capture the symmetry properties of

the system and display characteristic sign changes depending on the magnetic order.

Figure 3(g) presents the total energy of case (C) with the SCDF-T-BR89-CS functional for all three magnetic configurations as a function of the lattice constant a relative to the total energy E_0 of the most stable magnetic configuration at each value of a . This can be directly compared to the overview of XC functionals in Fig. 4 of Ref. [75]. There are two phase transitions in close proximity around 4 Å, with a narrow region where AFM1 is the most stable magnetic structure. This is qualitatively similar to what is obtained with MGGA-R2SCAN (not shown), while in contrast, hybrid-HSE06 yields no phase transition, with AFM2 being the most stable magnetic structure throughout the considered range for a [75]. The pure density functionals, LSDA and GGA-PBE, yield one phase transition from FM in the high-pressure region to AFM2 under ambient pressure.

As mentioned, the magnetic transition as a function of pressure obtained by SCDF-T-BR89-CS closely resembles that of MGGA-R2SCAN. Furthermore, the collinear version of BR89-CS yields qualitatively the same behavior with both algorithms, the collinear spin-polarized and the traditional noncollinear algorithm. This again hints towards the zero-torque limit being a good approximation for MnO. Nevertheless, we want to closely inspect the differences in the total energy of cases (A) E_{sp} , (B) E_{ncl} , and (C) $E_{\text{SCDF-T}}$. Surprisingly, there are relevant energy differences between the three modes as elucidated in Fig. 3(h) and (i). The fact that the magnetic ground state as a function of the lattice constant does not depend on the mode is due to the large energy difference between the magnetic structures of roughly 50-300 meV/f.u.. In other words, we cannot generally expect that the magnetic ground state is the same for (A), (B), and (C) for other systems as elaborated below.

Figure 3(h) presents the total energy difference $E_{\text{ncl}} - E_{\text{sp}}$ between the traditional noncollinear and spin-polarized calculations, both using the collinear spin-polarized version of BR89-CS. We see that for all investigated magnetic configurations and lattice constants the traditional noncollinear calculations lead to lower total energies. This can trivially be understood in terms of constrained minimization: The collinear algorithm (A) can only access a subset of solutions of the noncollinear case (B). In other words, the noncollinear algorithm (B) has more degrees of freedom to minimize the total energy and should strictly yield equal or lower total energy compared to the collinear algorithm (A) within the same XC functional.

We note that the energy difference in this system varies between -18 meV/f.u. and -0.8 meV/f.u., which is surprisingly large for a system where we expected this difference to vanish. It strongly depends on the magnetic configuration and the applied pressure. Hence, the relative stability of magnetic states changes, and in systems with almost degenerate magnetic configurations, this could change the predicted magnetic ground state.

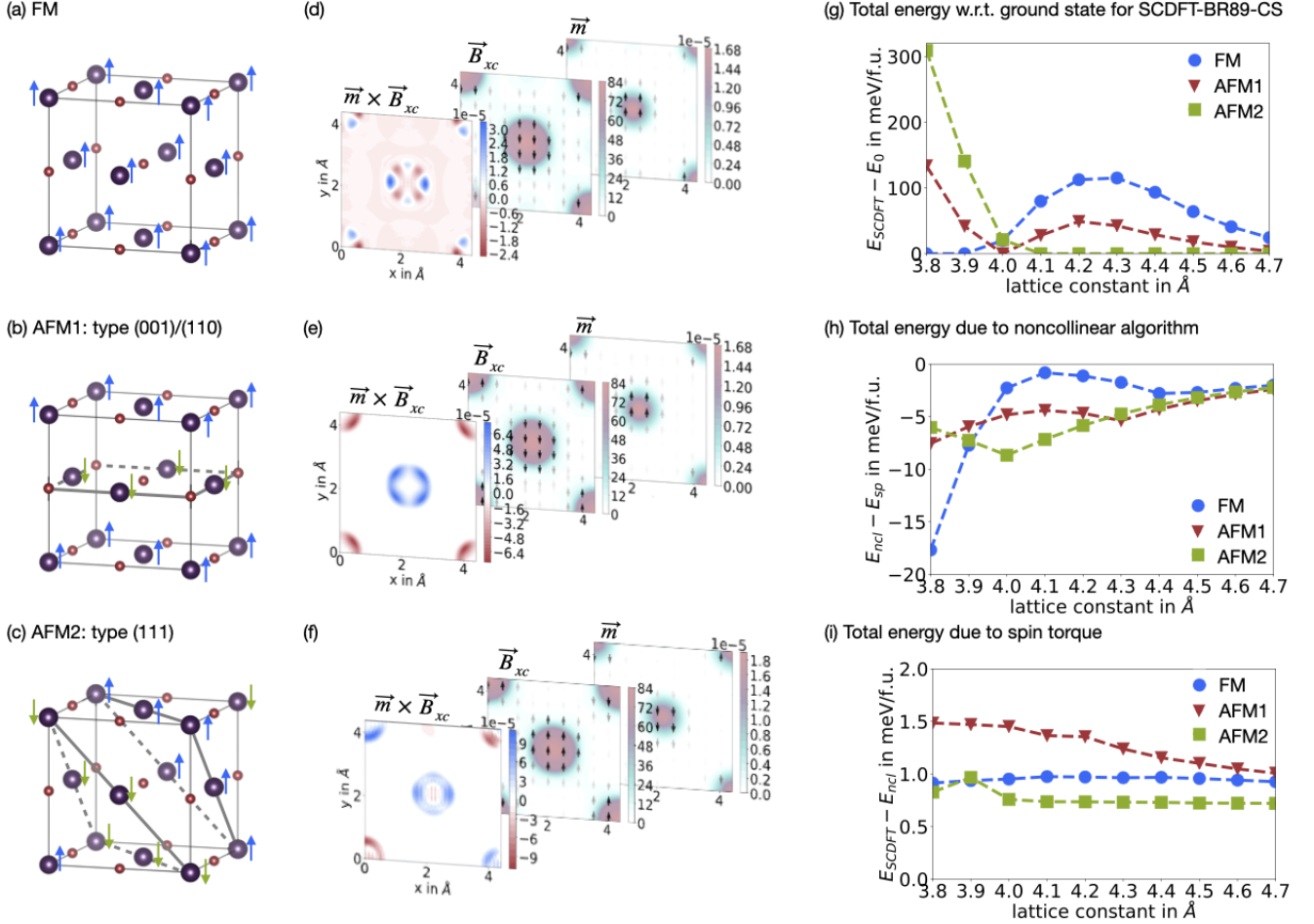


FIG. 3. Magnetic configurations of MnO: (a) FM, (b) AFM1 [type (001)/(110)], and (c) AFM2 [type (111)]. (d)-(f) Spin torque, XC B-field, and magnetization of the FM, AFM1, and AFM2 configurations, respectively, obtained from SCDFE-BR89-CS. (g) Total energy per formula unit of SCDFE-BR89-CS with respect to the ground state at the given lattice constant a as a function of a . (h) Total energy difference between the spin-polarized and the noncollinear algorithm using the spin-polarized MGGA-BR89-CS functional. (i) Total energy difference between the spin-polarized and the noncollinear versions of the BR89-CS functional within the noncollinear algorithm.

Moreover, in systems with itinerant electron magnetism with noncollinear magnetization in the interstitial regions the difference between the collinear algorithm and noncollinear algorithm is expected to be much larger. This is already seen in the present data: The FM solution at lattice constant $a \leq 3.9$ Å is metallic, while it is insulating for larger values of a . The metallic systems show a large total energy difference despite the fact that the magnetization is FM.

Next, let us compare (B) the traditional noncollinear algorithm using MGGA-BR89-CS and (C) the noncollinear SCDFE-BR89-CS. Considering the data in Fig. 3 (i), we find that the total energy obtained with SCDFE-BR89-CS is strictly higher than in the traditional noncollinear MGGA-BR89-CS calculation. We may understand this in terms of constrained minimization, since indeed, the spin-torque algorithm constrains the system to a physical subset of spin-densities with

a certain spin-current density and spin torque. Importantly, we see that the energy difference $E_{\text{SCDFE}} - E_{\text{ncl}}$ depends on the magnetic configuration. Hence, including spin-torque effects changes the relative stability of magnetic configurations and thus potentially changes the magnetic ground state. We also see that compared to Cr₃, where the energy difference is 0.05 eV, the effect is 50 times smaller, but not five orders of magnitude smaller than one may expect based on the spin torque.

Comparing Fig. 3 (h) and (i), $E_{\text{SCDFE}} - E_{\text{ncl}}$ is an order of magnitude smaller than $E_{\text{ncl}} - E_{\text{sp}}$. Hence, the spin-torque algorithm still yields equal or smaller total energies compared to the collinear algorithm. We also note that the spin-torque algorithm using the SCDFE-BR89-CS functional converges in fewer electronic minimization steps than the noncollinear algorithm. In fact, the spin-torque algorithm is as stable as the collinear algorithm, while the noncollinear algorithm takes about 3

TABLE II. Properties of MnO calculated with various XC functionals using either (A) the collinear algorithm, (B) the traditional noncollinear algorithm neglecting spin torque, or (C) noncollinear algorithm within SCDFE including spin torque. The columns correspond to the equilibrium lattice constant a_0 , the equilibrium lattice volume V_0 , the bulk modulus B_0 , and the on-site magnetic moment μ .

Case	XC functional	Algorithm	a_0 (Å)	V_0 (Å ³)	B_0 (GPa)	μ (μ_B)
1	LSDA	(A) collinear	4.32	80	155	4.14
2	MGGA-R2SCAN	(A) collinear	4.42	86	172	4.36
3	MGGA-R2SCAN	(B) noncollinear	4.42	86	172	4.36
4	MGGA-BR89-CS	(A) collinear	4.30	79	197	4.38
5	MGGA-BR89-CS	(B) noncollinear	4.30	79	198	4.38
6	SCDFE-BR89-CS	(C) spin-torque	4.30	79	198	4.38
7	Hybrid-HSE06	(A) collinear	4.44	87	164	4.48
Experiment			4.43 ^a	87 ^b	151 ^c , 162 ^d	4.54 ^e

^a Reference [71]

^b Reference [71]

^c Reference [72]

^d Reference [73]

^e Reference [74]

times as many electronic steps for MnO. The instability of the noncollinear algorithm is likely due to the ad hoc zero local spin-torque approximation which leads to inconsistencies between the energy and the potential. The same inconsistencies are present for the collinear algorithm, however it has much fewer degrees of freedom and is thus less prone to convergence issues.

Turning now to the results in Table II, we see that the lattice constant a_0 , bulk modulus B_0 , and on-site magnetic moment μ are sensitive to the choice of the XC functional, as expected, but almost independent of the choice of the algorithm (A)-(C). Similar to LSDA, the SCDFE/MGGA-BR89-CS functional significantly underestimates the equilibrium lattice constant a_0 for MnO by more than 3%, while MGGA-R2SCAN and hybrid-HSE06 yield very good predictions for a_0 with less than 0.3% of error. In addition, hybrid-HSE06 leads to a very good estimate for the bulk modulus B_0 and the on-site magnetic moment. The magnetic moments are quite accurately estimated by the BR89-CS functional, as well. To show the influence of the algorithm more significant digits are presented for R2SCAN (cases 2-3) and BR89-CS (cases 4-6). However, those go beyond the accuracy of measurement in both, the calculation and experiment, e.g., due to ambiguities in the definition of the on-site moment.

In summary, the results for MnO show that most of the physics in collinear magnetic systems without SOC is already captured by a collinear algorithm and the effects of the choice of the XC functional is much larger. The BR89-CS functional fails to describe accurately structural parameters, however it is the only XC functional thus far available in the framework of SCDFE. Nevertheless, the SCDFE-BR89-CS functional yields a characteristic behavior in the spin torque and it converges exceptionally well.

IV. CONCLUSION

We have shown the first ever consistent noncollinear ab-initio calculation using a $U(1) \times SU(2)$ gauge-invariant noncollinear semilocal XC functional, with a variational problem that is extended by the variation with respect to the components of the 2×2 paramagnetic spin-current density. The novel XC functional is formulated within SCDFE and cures the lack of spin torque in semilocal XC functionals. For the Cr₃ molecule we have shown that the spin torque is quite similar to the one obtained by EXX-KLI [20].

Our spin-torque calculations fundamentally differ from traditional noncollinear calculations [1, 2] since the latter are based on collinear XC functionals. These traditional noncollinear calculations introduce an ad hoc zero local spin-torque approximation which introduces an inconsistency between XC energy and XC potential that may lead to problems for the electronic convergence even in cases where the approximation is small. For instance, in MnO the total energy correction due to the local spin torque is merely of the order of 1 meV/f.u., while the spin-torque algorithm needs roughly a third of the number of steps in the electronic minimization compared to the traditional noncollinear algorithm. In magnetic systems with noncollinear magnetic order, the influence on the total energy due to neglecting spin torque can be much larger and potentially changes the magnetic ground state. For example in Cr₃, the total energy due to spin torque is 50 meV, which is well above the common energy differences between different magnetic orders [76].

Collinear XC functionals should be derived from SCDFE by setting the off-diagonal terms of the 2×2 quantities to zero instead of the commonly employed spin-scaling relation. That is because collinear systems also disobey exact spin scaling unless they are homoge-

neous electron gases, i.e., a pure spin-up or spin-down state. The expressions for our novel implementation are based on the Becke-Roussel exchange and Colle-Salvetti correlation functionals. It depends on the 2×2 spin density, kinetic-energy density, and spin-current density. The implementation in VASP entails computing the paramagnetic spin-current density within the PAW method and extending the variational problem to vary the total energy with respect to the density current, which makes it computationally slightly more demanding than MGGA calculations.

While the ad hoc zero local spin-torque approximation strongly affects the total energy and convergence properties, the on-site magnetic moment and lattice parameters are not sensitive to it for the investigated systems. In other words, traditional noncollinear and collinear al-

gorithms yield the same lattice constant, bulk modulus, and magnetic moment. This is good news because established XC functionals are promising candidates to be extended to SCDFT in order to cure the lack of spin torque, bad electronic convergence, and the discrepancy between the experiment and the total energy landscape of SCDFT while still yielding satisfying results for other properties.

For future work, several directions are worth exploring. On the one hand, there is a plethora of magnetic phenomena that may be sensitive to the zero local spin-torque approximation. On the other hand, more established XC functionals should be extended to the framework of SCDFT to allow for $U(1) \times SU(2)$ gauge-invariant noncollinear calculations without resorting to the ad hoc local zero spin-torque approximation.

-
- [1] J. Kübler, K.-H. Höck, J. Sticht, and A. Williams, Local spin-density functional theory of noncollinear magnetism, *J. Appl. Phys.* **63**, 3482 (1988).
- [2] J. Kübler, K.-H. Hock, J. Sticht, and A. Williams, Density functional theory of non-collinear magnetism, *J. Phys. F* **18**, 469 (1988).
- [3] W. Kohn and L. J. Sham, Self-consistent equations including exchange and correlation effects, *Phys. Rev.* **140**, A1133 (1965).
- [4] P. Hohenberg and W. Kohn, Inhomogeneous electron gas, *Phys. Rev.* **136**, B864 (1964).
- [5] J. P. Perdew and K. Schmidt, Jacob's ladder of density functional approximations for the exchange-correlation energy, *AIP Conf. Proc.* **577**, 1 (2001).
- [6] L. Kleinman, Density functional for noncollinear magnetic systems, *Phys. Rev. B* **59**, 3314 (1999).
- [7] D. Bylander and L. Kleinman, Full-potential generalized gradient approximation calculations of spiral spin-density waves in γ -Fe, *Phys. Rev. B* **59**, 6278 (1999).
- [8] K. Capelle and E. Gross, Spin-density functionals from current-density functional theory and vice versa: A road towards new approximations, *Phys. Rev. Lett.* **78**, 1872 (1997).
- [9] K. Capelle and L. N. Oliveira, Density-functional theory for spin-density waves and antiferromagnetic systems, *Phys. Rev. B* **61**, 15228 (2000).
- [10] K. Capelle, G. Vignale, and B. Györfy, Spin currents and spin dynamics in time-dependent density-functional theory, *Phys. Rev. Lett.* **87**, 206403 (2001).
- [11] S. Sen and E. I. Tellgren, A local tensor that unifies kinetic energy density and vorticity in density functional theory, *J. Chem. Phys.* **149**, 144109 (2018).
- [12] E. Trushin and A. Görling, Spin-current density-functional theory for a correct treatment of spin-orbit interactions and its application to topological phase transitions, *Phys. Rev. B* **98**, 205137 (2018).
- [13] T. J. P. Irons, G. David, and A. M. Teale, Optimizing molecular geometries in strong magnetic fields, *J. Chem. Theory Comput.* **17**, 2166 (2021).
- [14] C. Holzer, Y. J. Franzke, and A. Pausch, Current density functional framework for spin-orbit coupling, *J. Chem. Phys.* **157**, 204102 (2022).
- [15] Y. J. Franzke and C. Holzer, Current density functional framework for spin-orbit coupling: Extension to periodic systems, *J. Chem. Phys.* **160**, 184101 (2024).
- [16] R. Richter, T. Aschebrock, I. Schelter, and S. Kümmel, Meta-generalized gradient approximations in time dependent generalized Kohn-Sham theory: Importance of the current density correction, *J. Chem. Phys.* **159**, 124117 (2023).
- [17] R. T. Sharp and G. K. Horton, A variational approach to the unipotential many-electron problem, *Phys. Rev.* **90**, 317 (1953).
- [18] J. D. Talman and W. F. Shadwick, Optimized effective atomic central potential, *Phys. Rev. A* **14**, 36 (1976).
- [19] S. Sharma, J. K. Dewhurst, C. Ambrosch-Draxl, S. Kurth, N. Helbig, S. Pittalis, S. Shallcross, L. Nordström, and E. Gross, First-principles approach to noncollinear magnetism: Towards spin dynamics, *Phys. Rev. Lett.* **98**, 196405 (2007).
- [20] N. Tancogne-Dejean, A. Rubio, and C. A. Ullrich, Constructing semilocal approximations for noncollinear spin density functional theory featuring exchange-correlation torques, *Phys. Rev. B* **107**, 165111 (2023).
- [21] N. Tancogne-Dejean, A. Rubio, and C. A. Ullrich, Erratum: Constructing semilocal approximations for noncollinear spin density functional theory featuring exchange-correlation torques [phys. rev. b 107, 165111 (2023)], *Phys. Rev. B* **110**, 199902 (2024).
- [22] J. C. Slater, A simplification of the hartree-fock method, *Phys. Rev.* **81**, 385 (1951).
- [23] C. A. Ullrich, Density-functional theory for systems with noncollinear spin: Orbital-dependent exchange-correlation functionals and their application to the hubbard dimer, *Phys. Rev. B* **98**, 035140 (2018).
- [24] J. Krieger, Y. Li, and G. Iafrate, Construction and application of an accurate local spin-polarized kohn-sham potential with integer discontinuity: Exchange-only theory, *Phys. Rev. A* **45**, 101 (1992).
- [25] E. Sjöstedt and L. Nordström, Noncollinear full-potential studies of γ -Fe, *Phys. Rev. B* **66**, 014447 (2002).
- [26] M. Katsnelson and V. Antropov, Spin angular gradient approximation in the density functional theory, *Phys. Rev. B* **67**, 140406 (2003).

- [27] K. Capelle and B. L. Gyorffy, Exploring dynamical magnetism with time-dependent density-functional theory: From spin fluctuations to gilbert damping, *Europhys. Lett.* **61**, 354 (2003).
- [28] K. Bencheikh, Spin-orbit coupling in the spin-current-density-functional theory, *J. Phys. A: Math. Theor.* **36**, 11929 (2003).
- [29] J. E. Peralta, G. E. Scuseria, and M. J. Frisch, Noncollinear magnetism in density functional calculations, *Phys. Rev. B* **75**, 125119 (2007).
- [30] G. Scalmani and M. J. Frisch, A new approach to noncollinear spin density functional theory beyond the local density approximation, *J. Chem. Theory Comput.* **8**, 2193 (2012).
- [31] I. W. Bulik, G. Scalmani, M. J. Frisch, and G. E. Scuseria, Noncollinear density functional theory having proper invariance and local torque properties, *Phys. Rev. B* **87**, 035117 (2013).
- [32] F. G. Eich and E. K. U. Gross, Transverse spin-gradient functional for noncollinear spin-density-functional theory, *Phys. Rev. Lett.* **111**, 156401 (2013).
- [33] S. Sharma, E. Gross, A. Sanna, and J. Dewhurst, Source-free exchange-correlation magnetic fields in density functional theory, *J. Chem. Theory Comput.* **14**, 1247 (2018).
- [34] Z. Pu, H. Li, N. Zhang, H. Jiang, Y. Gao, Y. Xiao, Q. Sun, Y. Zhang, and S. Shao, Noncollinear density functional theory, *Phys. Rev. Res.* **5**, 013036 (2023).
- [35] S. Pittalis, G. Vignale, and F. Eich, $U(1) \times su(2)$ gauge invariance made simple for density functional approximations, *Phys. Rev. B* **96**, 035141 (2017).
- [36] J. K. Desmarais, J.-P. Flament, and A. Erba, Adiabatic connection in spin-current density functional theory, *Phys. Rev. B* **102**, 235118 (2020).
- [37] J. K. Desmarais, G. Ambrogio, G. Vignale, A. Erba, and S. Pittalis, Generalized kohn-sham approach for the electronic band structure of spin-orbit coupled materials, *Phys. Rev. Mater.* **8**, 013802 (2024).
- [38] J. K. Desmarais, G. Vignale, K. Bencheikh, A. Erba, and S. Pittalis, Electron localization function for noncollinear spins, *Phys. Rev. Lett.* **133**, 136401 (2024).
- [39] J. K. Desmarais, A. Erba, G. Vignale, and S. Pittalis, Meta-generalized-gradient approximation made magnetic, arXiv preprint arXiv:2409.15201 10.48550/arXiv.2409.15201 (2024).
- [40] J. K. Desmarais, J. Maul, B. Civalleri, A. Erba, G. Vignale, and S. Pittalis, Spin currents via the gauge principle for meta-generalized gradient exchange-correlation functionals, *Phys. Rev. Lett.* **132**, 256401 (2024).
- [41] J. Sun, A. Ruzsinszky, and J. P. Perdew, Strongly constrained and appropriately normed semilocal density functional, *Phys. Rev. Lett.* **115**, 036402 (2015).
- [42] A. P. Bartók and J. R. Yates, Regularized scan functional, *J. Chem. Phys.* **150**, 161101 (2019).
- [43] J. W. Furness, A. D. Kaplan, J. Ning, J. P. Perdew, and J. Sun, Accurate and numerically efficient r2scan meta-generalized gradient approximation, *J. Phys. Chem. Lett.* **11**, 8208 (2020).
- [44] G. Kresse and J. Hafner, Ab initio molecular dynamics for liquid metals, *Phys. Rev. B* **47**, 558 (1993).
- [45] G. Kresse and J. Hafner, Ab initio molecular-dynamics simulation of the liquid-metal-amorphous-semiconductor transition in germanium, *Phys. Rev. B* **49**, 14251 (1994).
- [46] P. E. Blöchl, Projector augmented-wave method, *Phys. Rev. B* **50**, 17953 (1994).
- [47] G. Kresse and D. Joubert, From ultrasoft pseudopotentials to the projector augmented-wave method, *Phys. Rev. B* **59**, 1758 (1999).
- [48] D. Hobbs, G. Kresse, and J. Hafner, Fully unconstrained noncollinear magnetism within the projector augmented-wave method, *Phys. Rev. B* **62**, 11556 (2000).
- [49] J. Sun, M. Marsman, G. I. Csonka, A. Ruzsinszky, P. Hao, Y.-S. Kim, G. Kresse, and J. P. Perdew, Self-consistent meta-generalized gradient approximation within the projector-augmented-wave method, *Phys. Rev. B* **84**, 035117 (2011).
- [50] M. Levy, Electron densities in search of hamiltonians, *Phys. Rev. A* **26**, 1200 (1982).
- [51] E. H. Lieb, Density functionals for coulomb systems, *Int. J. Quantum Chem.* **24**, 243 (1983).
- [52] D. Mejia-Rodriguez and S. B. Trickey, Deorbitalization strategies for meta-generalized-gradient-approximation exchange-correlation functionals, *Phys. Rev. A* **96**, 052512 (2017).
- [53] A. D. Becke and M. R. Roussel, Exchange holes in inhomogeneous systems: A coordinate-space model, *Phys. Rev. A* **39**, 3761 (1989).
- [54] R. Colle and O. Salvetti, Approximate calculation of the correlation energy for the closed shells, *Theor. Chim. Acta* **37**, 329 (1975).
- [55] Q_x with $\gamma = 1$ corresponds to Eq. (27) in Ref. [35].
- [56] The evaluation of the gradient should be understood as follows: $\tau_W^{\text{ncl}}(\mathbf{r}) = \frac{\sum_{\sigma\sigma'} \nabla' n_{\sigma\sigma'}(\mathbf{r}') \big|_{\mathbf{r}'=\mathbf{r}} \cdot \nabla'' n_{\sigma\sigma'}(\mathbf{r}'') \big|_{\mathbf{r}''=\mathbf{r}}}{8n}$.
- [57] R. McWeeny, Some recent advances in density matrix theory, *Rev. Mod. Phys.* **32**, 335 (1960).
- [58] C. Lee, W. Yang, and R. G. Parr, Development of the colle-salvetti correlation-energy formula into a functional of the electron density, *Phys. Rev. B* **37**, 785 (1988).
- [59] Mind the factor 1/2 in the definition of the kinetic-energy density and in the two-electron reduced density matrix.
- [60] G. L. Oliver and J. P. Perdew, Spin-density gradient expansion for the kinetic energy, *Phys. Rev. A* **20**, 397 (1979).
- [61] This occurred in the implementation reported in [20, 21]: In the BR89 exchange energy [53], one introduces a γ factor that only acts on the kinetic-energy density and not on the Laplacian term. However, the substitution employed in [20, 21] introduces the off-diagonal terms of the Laplacian by substituting the kinetic-energy density. We still commend this pioneering work as it inspired us to tackle the implementation.
- [62] P. A. M. Dirac, Note on exchange phenomena in the thomas atom, *Math. Proc. Cambridge Philos. Soc.* **26**, 376 (1930).
- [63] J. P. Perdew and A. Zunger, Self-interaction correction to density-functional approximations for many-electron systems, *Phys. Rev. B* **23**, 5048 (1981).
- [64] D. M. Ceperley and B. J. Alder, Ground state of the electron gas by a stochastic method, *Phys. Rev. Lett.* **45**, 566 (1980).
- [65] J. P. Perdew, K. Burke, and M. Ernzerhof, Generalized gradient approximation made simple, *Phys. Rev. Lett.* **77**, 3865 (1996).
- [66] J. Heyd, G. E. Scuseria, and M. Ernzerhof, Hybrid functionals based on a screened coulomb potential, *J. Chem. Phys.* **118**, 8207 (2003).
- [67] A. V. Krukau, O. A. Vydrov, A. F. Izmaylov, and G. E. Scuseria, Influence of the exchange screening parame-

- ter on the performance of screened hybrid functionals, *J. Chem. Phys.* **125**, 224106 (2006).
- [68] M. Marsman, J. Paier, A. Stroppa, and G. Kresse, Hybrid functionals applied to extended systems, *J. Phys.: Condens. Matter* **20**, 064201 (2008).
- [69] Y. Fu and D. J. Singh, Density functional methods for the magnetism of transition metals: Scan in relation to other functionals, *Phys. Rev. B* **100**, 045126 (2019).
- [70] F. Tran, G. Baudesson, J. Carrete, G. K. H. Madsen, P. Blaha, K. Schwarz, and D. J. Singh, Shortcomings of meta-gga functionals when describing magnetism, *Phys. Rev. B* **102**, 024407 (2020).
- [71] S. Sasaki, K. Fujino, Y. Takeuchi, and R. Sadanaga, On the estimation of atomic charges by the x-ray method for some oxides and silicates, *Acta Crystallogr. A* **36**, 904 (1980).
- [72] Y. Noguchi, K. Kusaba, K. Fukuoka, and Y. Syono, Shock-induced phase transition of mno around 90gpa, *Geophys. Res. Lett.* **23**, 1469 (1996).
- [73] R. Jeanloz and A. Rudy, Static compression of mno manganosite to 60 gpa, *J. Geophys. Res.* **92**, 11433 (1987).
- [74] W. Jauch and M. Reehuis, Electron density distribution in paramagnetic and antiferromagnetic mno: A γ -ray diffraction study, *Phys. Rev. B* **67**, 184420 (2003).
- [75] T. Archer, C. Pemmaraju, S. Sanvito, C. Franchini, J. He, A. Filippetti, P. Delugas, D. Puggioni, V. Fiorentini, R. Tiwari, *et al.*, Exchange interactions and magnetic phases of transition metal oxides: Benchmarking advanced ab initio methods, *Phys. Rev. B* **84**, 115114 (2011).
- [76] M.-T. Huebsch, T. Nomoto, M.-T. Suzuki, and R. Arita, Benchmark for ab initio prediction of magnetic structures based on cluster-multipole theory, *Phys. Rev. X* **11**, 011031 (2021).